PHYSICAL REVIEW E **68**, 065301(R) (2003)

Scaling evolution in shock-induced transition to turbulence

P. Vorobieff and N.-G. Mohamed
The University of New Mexico, Albuquerque, New Mexico 87131, USA

C. Tomkins, C. Goodenough, M. Marr-Lyon, and R. F. Benjamin
Los Alamos National Laboratory, Los Alamos, New Mexico 87544, USA

(Received 26 March 2003; published 23 December 2003)

In this experimental study, a column of heavy gas (SF_6) surrounded by light gas (air) is accelerated by a planar Mach 1.2 shock. Richtmyer-Meshkov instability on the initially diffuse air-SF_6 interface determines the repeatable large-scale vortex dynamics of the system after the shock passage. Subsequently secondary instabilities form, with the system eventually transitioning to turbulence. We present highly resolved measurements of two components of the instantaneous velocity fields. With these measurements, we investigate the evolution of velocity statistics over a substantial range of scales in terms of structure functions. The latter evolve to exhibit late-time behavior consistent with the Kolmogorov scaling law for fully developed turbulence, despite the transitional character, anisotropy, and inhomogeneity of our flow. Ensemble averaging and comparison with instantaneous results reveal a trend towards the same scaling manifested much earlier by the structure functions of the fluctuating velocity components.

DOI: 10.1103/PhysRevE.68.065301 PACS number(s): 47.20.Ma, 47.20.Ky, 47.27.−i, 47.40.Nm

The Richtmyer-Meshkov instability (RMI) [1,2] develops when a shock wave traverses a density interface (sharp or diffuse) separating two gases. Misalignment between pressure and density gradients leads to vorticity production on the interface. Subsequently, the flow driven by the initially deposited vorticity leads to nonlinear instability growth and eventually to turbulence. RMI is important in many areas of physics—from geophysical and astrophysical problems such as stellar evolution [3] and transient events in Earth's magnetosphere [4] to applications including inertial confinement fusion [5] and supersonic combustion [6].

RMI also makes an attractive test case for the general problem of transition to turbulence. The initial conditions can be characterized in detail. The Reynolds number is sufficiently high to trigger the transition. The energy input driving the instability is finite and short timed in comparison with the interval between the shock interaction and the onset of turbulence. RMI studies have also served as a testbed for numerical code validation, with comparison between experimental and numerical results employed to ensure that the numerical codes faithfully reproduce the relevant physical processes.

Recent experiments have revealed many features of the evolution of RMI-driven flow transitioning to turbulence. After a short interval of linear instability growth described by Richtmyer [1], the flow enters a deterministic, vortex-dominated, nonlinear stage. Later on, secondary instabilities develop, adding a disordered component to the flow. Subsequently, the onset of turbulence is observed, with greatly enhanced mixing in the flow [7,8], multiple scales emerging [7,9], and the statistical and geometrical properties of the scalar field advected by the flow approaching those associated with fully developed turbulence [10,11].

Several theoretical models of the deterministic vortex dynamics due to RMI (e.g., Refs. [12–14]) are in good agreement with experiment. The deterministic large-scale structure of the flow is also reliably reproduced numerically [15]. The challenge for codes is to accurately simulate the small-scale, disordered features driven by shear and baroclinic [16] instabilities.

In this Rapid Communication, we present experimental measurements of the velocity field produced by accelerating a gas cylinder (Fig. 1) with a Mach 1.2 shock. We quantify not only the large-scale structure of the velocity field, but the contribution of the secondary instabilities as well.

As the flow begins the transition to turbulence, the velocity structure functions evolve to exhibit behavior consistent with the Kolmogorov theory for fully developed turbulence [17], specifically, with the 2/3 scaling law, the transitional and nonisotropic character of the system notwithstanding. Results from earlier work with different initial conditions [10] suggested that the velocity field might develop turbulent statistics, as the passive scalar tracer advected by the flow developed Obukhov-Corrsin [18] scaling consistent with turbulence, however, this is the first direct measurement, to the best of our knowledge.

High repeatability of our experiment unattainable in earlier work [7,10,11] allows ensemble-averaging based decomposition of the flow fields into deterministic and disordered components. We find significant differences in the scaling of the former and the latter: the disordered velocity components likely associated with secondary flow instabilities develop Kolmogorov-like scaling much earlier than the overall velocity field.

The experiments were conducted in a horizontal, square

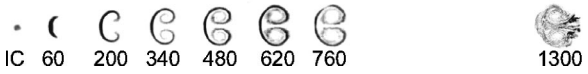

FIG. 1. Composite laser-sheet visualization of the shock-accelerated gas cylinder evolution. Direction of the flow is from left to right. ''IC'' denotes initial conditions, timings of subsequent dynamic exposures (microseconds after initial acceleration) are labeled.

75-mm cross-section shock tube [7] with optical windows and an interchangeable injection nozzle in the test section to generate a variety of initial conditions. A vertical, gravity-driven flow of sulfur hexafluoride (SF_6) enters the test section through the nozzle at the top surface of the test section and exits through a slit at the bottom, thus forming a diffuse interface with the air that fills the tube.

In the experiments presented here, the nozzle cross section was round with a 3.1 mm diameter, producing a vertical gas cylinder in the test section. The air and/or SF_6 can be seeded with submicron-sized glycol vapor droplets. The flow is illuminated by a pair of Nd:YAG (yttrium-aluminum-garnet) lasers (one custom multiple-pulsed, the other commercial single- or double-pulsed) producing a horizontal light sheet ~ 2 cm below the nozzle, at about 2/3 of the height of the test section. A Mach 1.2 shock (400 m/s front velocity, 100 m/s piston velocity) accelerates the flow, initiating RMI. Figure 1 shows a composite image of flow visualization acquired with SF_6 seeded with glycol (dark) and no tracer in the air (white background).

Flow images were acquired with three digital cameras: one for the initial conditions, the second for imaging the dynamics of flow evolution, and the third capable of high-resolution zoom-in on an area of the flow. In Fig. 1, the initial conditions are captured by the first camera, the first six dynamic images by the second camera, and the seventh, late-time dynamic image by the third camera. The third camera is capable of capturing two images with a time interval between them as small as 1 μs and resolving individual glycol droplets, thus permitting acquisition of a horizontal section of the instantaneous velocity field via particle-image velocimetry (PIV) [19]. We use a two-step algorithm with cross correlation followed by adaptive particle tracking. The flow-tracking fidelity of the glycol tracer is adequate for PIV [7,20], while the main limiting factor of velocity reconstruction accuracy is spatial resolution (8.3 μm per pixel). Since the diffraction-limited tracer spot size created by an imaged particle is smaller than the pixel resolution, we use defocusing to produce tracer images slightly larger than the pixel size. Thus we resolve subpixel scales [21], reducing the random displacement error to about 0.15 pixel sizes. The velocity fields analyzed in this paper (Fig. 2) were acquired with a 4-μs delay.

Our conservative estimate of random velocity reconstruction error is about 0.25 m/s or 0.25% of the piston velocity. The PIV interrogation of the 1008×1012-pixel bitmap pairs produces fields with about 16 000 vectors on an irregular grid, with the characteristic vector-to-vector distance ~ 70 μm. Thus the dynamic spatial range of the field measurements (i.e., the ratio of the largest spatial separation between data points to the smallest) slightly exceeds two decades and the dynamic velocity range (the ratio of the largest measurable velocity to the smallest) is of the same order. Only the velocity components in the plane of the laser sheet are acquired. Velocity measurements were taken at 480, 760, and 1300 μs after shock interaction with the gas cylinder.

The highly repeatable pattern of the flow evolution is apparent in Figs. 1 and 2. The initial interaction of the shock with the gas cylinder leads to rollup of two large-scale counterrotating vortices. As the flow evolves, secondary instabilities developing along the distorted interface cause formation of smaller-scale vortices. The effects of these vortices are apparent in the flow-visualization image in Fig. 2, and the vortices themselves are evident in the corresponding vorticity contour plot. At later times, structures due to the secondary instabilities appear more prominently.

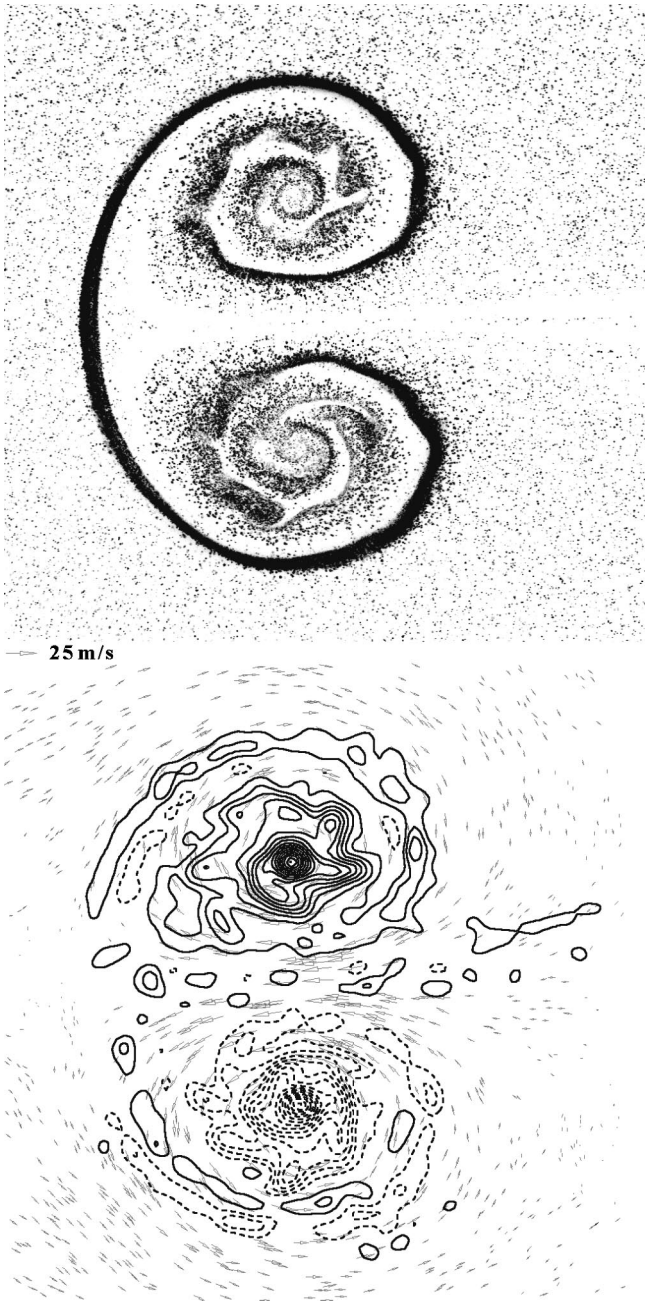

FIG. 2. Top: flow image at 760 μs after shock acceleration. Bottom: corresponding velocity field (arrows, piston velocity subtracted, no filtering, no interpolation, one in ten actual vectors shown) and vorticity contours (dashed—counterclockwise, solid—clockwise) fields. Vorticity contours plotted at $\pm1,\pm3,$ $\pm5,\ldots(s^{-1})$ velocity scale shown in the figure.

Having acquired at least 12 instantaneous velocity fields at each time (480, 760, and 1300 μs), we calculate the

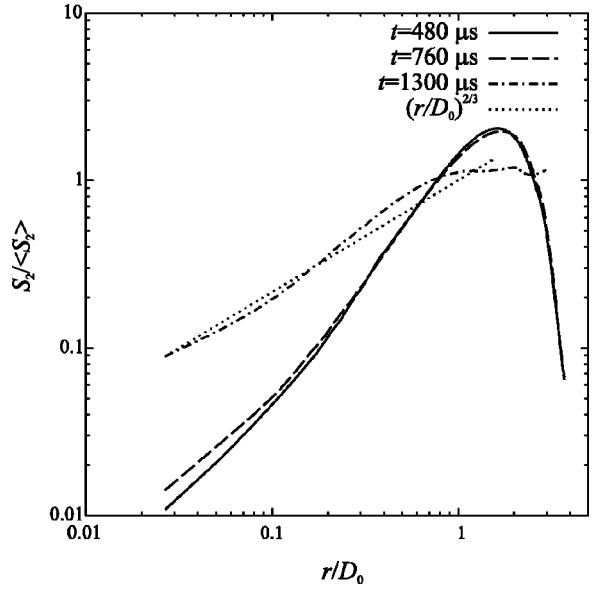

FIG. 3. Velocity structure function $S_2(r)$ evolution. r is normalized by the nozzle diameter D_0, S_2 at each time is normalized by its average value. Thin dotted line—$r^{2/3}$ slope.

second-order longitudinal velocity structure functions $S_2(r) = \langle([\mathbf{u}(\mathbf{x}+\mathbf{r})-\mathbf{u}(\mathbf{x})]\cdot\hat{\mathbf{r}})^2\rangle$, where $\langle\ \rangle$ denotes spatial averaging over every instantaneous velocity field and $\hat{\mathbf{r}}=\mathbf{r}/|\mathrm{r}|$. Figure 3 shows a comparison of the structure functions at three times.

At the two earlier times, the normalized structure functions are dominated by the peak apparently associated with the large-scale structure of the flow. There is some growth of the contribution of small scales between 480 and 760 μs. At 1300 μs, this contribution increases appreciably, and the slope of the structure-function plot becomes roughly consistent with the 2/3 power law of the Kolmogorov turbulence [17]. This respective growth of small scales as the flow transitions to turbulence should be attributable to secondary instabilities.

A significant new contribution to our knowledge of transition to turbulence would be information about the respective statistical properties of the deterministic part of the flow field (large-scale vortices driven by the initial baroclinic instability) and the disordered part (smaller-scale, secondary-instability-driven vortices). Ensemble averaging the instantaneous velocity fields should suppress the latter, but a smart averaging technique is required to minimize the effect of small jitter in exposure timing, which can lead to effective translation of the evolving gas cylinder by a distance noticeably larger than the smallest spatial scale we can resolve. Thus the ensemble-averaging procedure for the velocity fields was implemented as follows. First, for each instantaneous velocity field we obtained the corresponding field of enstrophy Ω (vorticity squared). Then we determined the ''center of enstrophy'' (x_Ω, y_Ω), which is analogous to the center of gravity in solid mechanics:

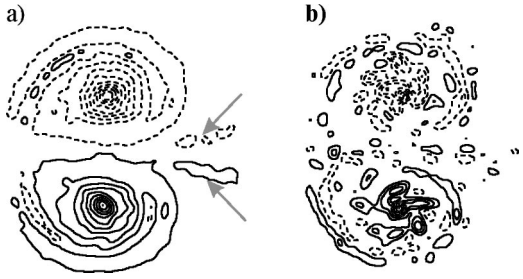

FIG. 4. Ensemble-averaged vorticity field at 760 μs [left (a)] and vorticity fluctuation field [right (b)] produced by subtracting the ensemble average from the vorticity shown in Fig. 2. Vorticity contours are plotted the same way as in Fig. 2. Gray arrows denote vorticity concentrations downstream of the large-scale vortex pair.

$$x_\Omega = \frac{\sum_k \Omega_k x_k}{\sum_k \Omega_k}, \quad y_\Omega = \frac{\sum_k \Omega_k y_k}{\sum_k \Omega_k},$$

with k denoting each grid point. Each instantaneous velocity field was translated to center (x_Ω, y_Ω). Then the fields were ensemble averaged. Figure 4 shows the results based on ensemble averaging of 12 fields, but the procedure begins to converge after nine fields (relative difference between the averaged vorticity for 9 and 12 fields not exceeding 5%). Besides the large-scale vortex pair that one would expect to find, the ensemble averaged field reveals the existence of a pair of shear layers associated with the SF_6 ''mushroom cap.'' These correspond to bands of opposite-sign vorticity following the outline of the ''cap'' on the upstream (left) side

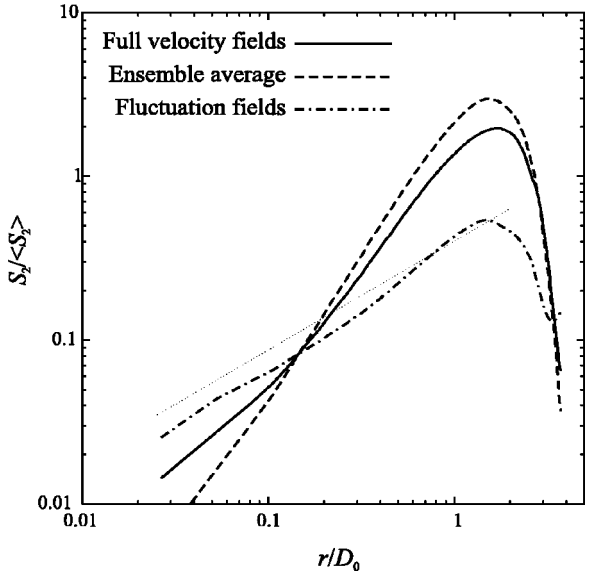

FIG. 5. Comparison of the longitudinal velocity structure function S_2 behavior at 760 μs for the original velocity fields, ensemble-averaged velocity, and velocity-fluctuation fields. The graphs are labeled in the plot. Normalization for all the graphs is based on S_2 for the original velocity field. Thin dotted line shows $r^{2/3}$ slope.

of the deforming gas column. The ensemble average also shows a pair of vorticity concentrations (arrows) on the downstream (right) side of the column, which were first observed in numerical simulations [22], but previously not reported in experiments.

Figure 4(b) shows the fluctuating components of velocity and vorticity obtained by subtracting the ensemble averages from the centered instantaneous fields. Inspection of the vorticity fluctuation fields reveals increased activity on the smaller scales, and vortices created by the secondary instabilities are much easier to distinguish. Figure 5 shows a comparison of the structure-function S_2 behavior for the ensemble-averaged and fluctuation fields at 760 μs. The overall behavior of the ensemble-averaged plot is very similar to that of the plot for the fields prior to decomposition. It is interesting that the fluctuation plot is much different, with a slope roughly consistent with the 2/3 power law. The intersection point of the ensemble-average and fluctuation structure functions should define a characteristic crossover scale, with energy on smaller scales carried predominantly by disordered flow structures, whereas the larger scales are dominated by the deterministic flow. The crossover scale at 760 μs is at or near $0.13D_0$. Similar analysis produces crossover scales $0.11D_0$ at 480 μs and $0.4D_0$ at 1300 μs. This increase of the crossover scale is consistent with the transition between early-time and late-time scaling. The early-time crossover scale is near the characteristic scale of vortices rolling up due to secondary instabilities. The influence of these disordered features appears to propagate to larger scales as the flow evolves towards turbulence.

It is also likely that the different scalings of the ensemble-averaged and fluctuation velocity are related to differences in the dimensionality of the mean and fluctuating flow. The initial conditions are spatially nearly two dimensional (2D), and thus the large-scale vortex structure due to the primary instability (RMI) is also predominantly 2D. The secondary instabilities are shear driven (Kelvin-Helmholtz) or baroclinic. In both cases, the rollup of secondary vortices would also occur in the direction of the primary vortex columns. At least for shear-driven rollup, however, recent analysis shows that the secondary vortices instantly lose stability in the spanwise direction, as well as become unstable due to a pairing instability, thus producing a ''one-step bifurcation to disorder'' [23]. This could explain the Kolmogorov-like velocity fluctuation structure function emerging well before the overall flow follows the same trend. Moreover, the vortex-pairing instability of the shear-driven small-scale vortices could be one of the mechanisms behind the increase of the crossover scale with time.

ACKNOWLEDGMENTS

This work was supported by the U.S. DOE under Contract No. W-7405-ENG-36. Special thanks are due to M. Briggs, K. P. Prestridge, and P. M. Rightley.

[1] R.D. Richtmyer, Commun. Pure Appl. Math. **8**, 297 (1960).
[2] E.E. Meshkov, Izv. Akad. Nauk SSSR, Mekh. Zhidk. Gaza **4**, 151 (1969) [Sov. Fluid Dyn. **4**, 101 (1969)].
[3] D. Arnett, Astrophys. J., Suppl. **127**, 213 (2000).
[4] C.C. Wu, J. Geophys. Res., [Space Phys.] **105**(A11), 7533 (2000).
[5] J.D. Lindl, R.L. McCrory, and E.M. Campbell, Phys. Today **45**, 32 (1992).
[6] J. Yang, T. Kubota, and E.E. Zukoski, AIAA J. **31**, 854 (1993).
[7] P.M. Rightley, P. Vorobieff, R. Martin, and R.F. Benjamin, Phys. Fluids **11**, 186 (1999).
[8] B.D. Collins and J.W. Jacobs, J. Fluid Mech. **464**, 113 (2002).
[9] G. Dimonte and M. Schneider, Phys. Plasmas **4**, 4347 (1997).
[10] P. Vorobieff, P.M. Rightley, and R.F. Benjamin, Phys. Rev. Lett. **81**, 2240 (1998).
[11] P. Vorobieff, P.M. Rightley, and R.F. Benjamin, Physica D **133**, 469 (1999).
[12] R. Samtaney and N. Zabusky, J. Fluid Mech. **269**, 45 (1994).
[13] J. Hecht, U. Alon, and D. Shvarts, Phys. Fluids **6**, 4019 (1994).
[14] Q. Zhang and S. Sohn, Phys. Fluids **9**, 1106 (1997).
[15] R.L. Holmes *et al.*, J. Fluid Mech. **389**, 55 (1999).
[16] A.W. Cook and Y. Zhou, Phys. Rev. E **66**, 026312 (2002).
[17] A.N. Kolmogorov, C. R. Acad. Sci. URSS **30**, 301 (1941).
[18] A.M. Obukhov, Izv. Akad. Nauk SSSR **13**, 58 (1949); S. Corrsin, J. Appl. Phys. **22**, 469 (1951).
[19] A.K. Prasad, Curr. Sci. **79**, 51 (2000).
[20] K. Prestridge, P. Vorobieff, P.M. Rightley, and R.F. Benjamin, Phys. Rev. Lett. **84**, 4353 (2000).
[21] A.K. Prasad, R.J. Adrian, C.C. Landreth, and P.W. Offutt, Exp. Fluids **13**, 105 (1992).
[22] W.J. Rider and J. Kamm (private communication).
[23] J.-M. Chomaz, Bull. Am. Phys. Soc. **47(10)**, 32 (2002).